# Inversion of refractions and reflections by full-waveform inversion for marine streamer data: Classification of problem types and solution methods

STEVE KELLY, JAIME RAMOS-MARTINEZ, KATHY ZOU, and BORIS TSIMELZON, PGS

We classify full-waveform inversion (FWI) projects according to the types of events used to invert marine streamer data. In general, an adequate model update requires the seamless introduction of wavenumbers that are missing in the starting model. It has been our experience that this may require extraction of the lowest possible wavenumbers from the data, as well as the application of preprocessing procedures and scattering kernels that are optimal for each type of arrival. In a shallow-water environment, and with sufficient offsets, refracted arrivals and diving waves can provide an adequate inversion for shallow velocity structures. We demonstrate this principle using the linearized (Born) scattering kernel for field data from the North Sea.

For depths below the deepest turning point of recorded refractions and diving waves, we show that reflections can also be used to advantage under Born scattering assumptions, if the signal-to-noise ratio of the data allows the use of exceptionally low frequencies, say down to 2 Hz. It is more common, however, to work with data that have good signal-to-noise ratio only for frequencies above 3–4 Hz. Under these circumstances, we show that deep reflections can still yield a useful inversion, provided that the velocity update is performed using a depth-integrated form of the reflectivity. For each iteration, this strategy adds nonlinearity to the velocity recovery, and it thus tolerates a starting model that is less accurate than that required using the Born scattering kernel. We demonstrate the application of this strategy for data from the Gulf of Mexico.

## Introduction

Several studies of field data over the last few years have demonstrated the versatility of full-waveform inversion (FWI) in resolving small-scale velocity features. Barkved et al. (2010) inverted OBC recordings above Valhall Field and identified channel features in the shallow sediments, as well as gas pockets that had distorted migrated images for underlying reflectors. They also demonstrated improved correlation between sonic field logs and isotropic velocities inverted by FWI, after stretching to account for anisotropy. Gholami et al. (2011) performed both single- and multiparameter, anisotropic inversions of the Valhall OBC data. Sheng et al. (2006) applied FWI to shallow diving waves recorded in the Gulf of Mexico in an attempt to invert for shallow gas pockets that distorted migrated images for deeper reflections. We show a similar example for shallow velocity heterogeneities in the North Sea.

In contrast to the encouraging results for shallow inversion work, there are few examples of successful waveform inversions for structures that lie below the deepest turning

point for recorded refractions and diving waves. The reason for this is that the signal-to-noise ratio of the lowest frequencies in marine streamer recordings may not be sufficient to allow a continuous velocity update for the range of spatial wavenumbers typically present in starting velocity models that have been derived using ray-based reflection and beam tomography. Kelly et al. (2010) introduced a method for enhancing the recovery of low wavenumbers by integrating the image for each iteration, in order to obtain the velocity perturbations over depth. This procedure recognizes the shortcomings of the Born approximation, and it adds nonlinearity to the solution within each iteration. In this article, we extend the application of this work to update velocities at a depth of 6 km for data acquired in the Gulf of Mexico. We also present an inversion example for data with exceptional signal-to-noise ratio that allowed the inversion of frequencies as low as 2 Hz. These low frequencies were used to update a very poor starting model and dramatically improve the flatness of CIP gathers.

## Inversion approach

In this section, we review the components of our inversion strategy, with an emphasis on those characteristics that are unique to our implementation. FWI is applied in an iterative manner, because wave propagation is a nonlinear function of Earth parameters and because the update for each iteration typically depends on a linearizing assumption. The details for application of FWI by reverse time migration are well known throughout the industry. Shot records are modeled by the two-way wave equation, and the difference between the modeled and recorded data i.e., the data residuals, are then back-propagated to form a subsurface image. A 90° phase shift is applied prior to back propagation. The cumulative image from all shots is then mapped into a spatial distribution for the velocity perturbation that is used to update the starting model. The above process is repeated until the L-2 norm of the data residuals for all the shots (objective function) satisfies a convergence criterion.

Within the above framework, we apply one of two different methods for mapping the image of each shot into a velocity perturbation. The choice of algorithm is dictated by the type of arrival in the data that we intend to invert. The algorithm most commonly applied in the industry has the form:

$$\delta V(\mathrm{x}) = [1/V^3(\mathrm{x})] \cdot \Gamma(\mathrm{x}), \qquad (1)$$

where $\delta V$ is the velocity perturbation and $\Gamma$ is the image normalized by the source power. This mapping is based on two key assumptions of linearized, diffraction tomography

(Wu and Toksoz, 1987). First, the velocity perturbation is assumed to be small with respect to the velocity of the starting model, i.e., $|\delta V(x)| \ll V(x)$. Second, the magnitude of the back-propagated, residual wavefield is small with respect to the magnitude of the incident wavefield. The second assumption is typically referred to as the Born approximation. It implies that the incident wave remains unchanged during propagation through the heterogeneity that is being imaged by the data residuals. The validity of the first approximation depends on the accuracy of the velocity magnitudes at each point in the starting model, while the validity of the second approximation depends on both the magnitude and the scale sizes of the velocity heterogeneities represented by the residuals. The larger the scale size of the heterogeneity, the less likely it is that the Born approximation is satisfied. Departures from these approximations represent nonlinearities between the model and the data that necessitate an iterative solution method.

The objective function for nonlinear problems typically has many minima, although only one minimum corresponds to the desired (global) solution. Practical inversion strategies thus incorporate procedures for inverting successive subsets of the data in order to guide the solution, as closely as possible, to the global minimum. Because a given starting model represents a smoothed representation of the desired solution, these procedures attempt to inject the longest possible wavelengths (smallest wavenumbers) in the early stages of an inversion, and successively larger wavenumbers in the later stages. Diving waves, refractions and reflections each possess different capabilities for improving the resolution of a model. In particular, each is capable of providing different ranges of minimum and maximum wavenumber. For a given plane-wave component of the source wavefield with radial frequency $\omega$ and wave vector $k^S$, and a given plane-wave component of the back-propagated, residuals wavefield with wavevector $k^{\delta R}$, the imaging condition in FWI injects a velocity perturbation that has wave vector $k^{\delta V}$ with magnitude:

$$| k^{\delta V} | = | k^S + k^{\delta R} |. \qquad (2)$$

For a starting model in which the velocity varies only with depth, Equations 19 of Sirgue and Pratt (2004) give the horizontal and vertical wavenumber components for the image of a reflection as:

$$k_x^{\delta V} = 0, \quad k_z^{\delta V} = 2\omega \cdot cos(\theta)/V, \qquad (3)$$

where $V$ is the velocity of the background model at the image point and $\theta$ is the incidence angle, measured with respect to the vertical. Equations 3 show that in a depth-dependent medium, the image of a reflection can only provide an improvement in vertical resolution. It also shows that if the vertical velocity variation in the starting model is missing long spatial wavelengths, (i.e., low wavenumbers), then the inversion must employ either low frequencies or large incidence angles. Velocity heterogeneities also give rise to phase delays that can be imaged by the data residuals using transmitted

energy. These images can improve both vertical and horizontal resolution, depending on the magnitude and direction of the wave vector for the resulting image (Equation 2). They can be constructed from diving waves, refractions and even reflections that originate beneath the location of the heterogeneity.

Diving waves and refractions can update the velocity model anywhere between the water bottom and their turning point in the subsurface. Unfortunately, typical acquisition spreads rarely extend beyond 8 km, so the diving waves and refractions available for inversion penetrate no more than a few kilometers below the sea surface. Shallow water provides the best environment for exploiting these data. In deep water, where diving waves and refractions may not be present, there is no alternative but to use reflections. Equation 3 for $k_z$ shows that these arrivals have only a limited ability to update the lowest wavenumbers. Under these circumstances, we have found it fruitful to treat the image of the residuals as a perturbation in reflectivity. The perturbation in velocity is then found by integrating this image over depth as:

$$\delta V( x ) = 2V( x ) \cdot \int_{x_0}^{x} \Gamma( x' )dx', \qquad (4)$$

where $V(x)$ is the velocity and $\delta V(x)$ is the perturbation in velocity at location $x$, and $\Gamma(x')$ is the cumulative image at $x'$ from all shots, normalized by the cumulative source power at $x'$. Ideally, the integration is performed along a path orthogonal to the velocity contours of the background model, beginning at the water bottom. However, in areas without significant structure, it is sufficient to perform it in the vertical direction. When Equation 4 is applied, we neglect the 90° phase shift of the residuals that is part of the data preparation for inversion by Equation 1.

The preconditioned gradient in Equation 4 has a greater range of applicability than the Born approximation for near-vertical propagation, because it extends the range of object sizes and removes some of the nonlinearity inherent in each iteration. Synthetics tests have shown that this method converges more rapidly than inversion by Equation 1. There are, however, two significant drawbacks. When this method is applied in conjunction with a scalar wave equation, all perturbations are assumed to originate solely from velocity contrasts. We enforce this assumption by applying mutes to the data that exclude reflections whose origin is likely the result of density contrasts (e.g., the reflection at the water bottom). Practical application of this approach also requires a careful filtering of the low wavenumbers that cannot satisfy Equation 3, because these wavenumbers represent noise that is boosted during the spatial integration.

In summary, we invert band-limited data with the lowest frequencies first, because the lowest frequencies provide the most linear behavior. If the data include sufficient diving waves and refractions, we apply the Born scattering kernel shown in Equation 1. The lowest wavenumbers are selectively inverted first by picking a mute above the first breaks and

then applying a time taper to window just the leading edge of the first arrivals. We extend the length of the taper for later inversion stages, which has the effect of accommodating higher wavenumbers. For inversion depths below the deepest turning point of any available diving waves and refractions, we first attempt to apply the Born scattering kernel. If the resulting update is "ringy" and its spectrum has prominent notches, then it is missing low wavenumbers, so we re-invert using Equation 4.

## An example of Born inversion using refractions and diving waves to resolve shallow channels

We first present an inversion example that resolves shallow channels, with dimensions of a few hundred meters, that lie at a depth range of 100–400 m below the water bottom. The water depth in this area is approximately 90–120 m. Under these conditions, reflection ray tomography performs poorly in resolving shallow structures, due to the limited range of available ray paths. Also, the shallow water multiples that are superimposed on the primary reflections inhibit inversion by reflection ray tomography and they are difficult to remove. Although these arrivals are present in the recorded data during FWI, they are also generated during the modeling step. Their presence in the data residual thus assists convergence of the inversion by providing additional information about the data fit.

The inversion of shallow structures in shallow water entails minimal preprocessing. Beginning with raw shot records, the key steps that are important for successful inversion of refractions in shallow water include editing and removal of coherent noise, conversion to minimum phase in order to assist the selection of a mute just above the first breaks, Butterworth minimum-phase filtering to the inversion bandwidth and, finally, definition of a shot-dependent mute pattern above the first breaks..

The data under investigation were acquired using dual-sensor streamers in the North Sea. The cable length was 5.1 km and the spacing between them was 100 m, with a total of 6 cables. The shot depth was 6 m and the cables were at a depth of 15 m. The starting model for FWI was obtained

through ray-based reflection tomography for vertical transversely isotropic (VTI) symmetry. During the inversion, only the velocity for vertical propagation was updated, while the remaining anisotropy parameters were held constant. The total bandwidth for the inversion extended from 3 to 10 Hz and included all but the very nearest offsets.

In this article, we only show inversion results from five sail lines that were chosen to demonstrate the potential capability of FWI to resolve small-scale channels in the shallow sediments. The inversion was constrained to allow a complete update over only the top 500 m of the model. Figure 1 shows the starting (upper panel) and inverted (lower panel)
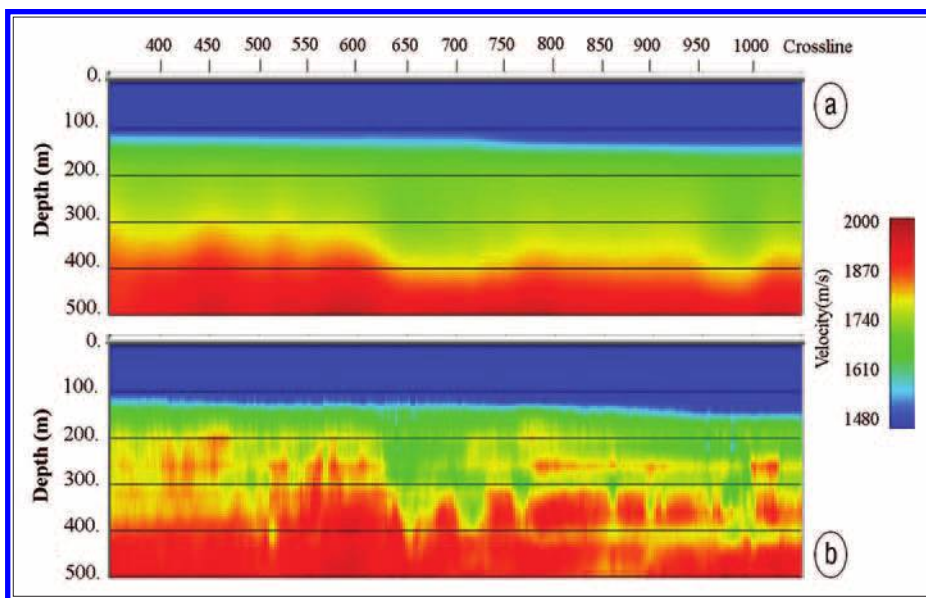


**Figure 1.** *Central inline of the velocity models before (a) and after (b) inversion. The inversion was constrained to allow a complete update over only the top 500 m of the model. The distance between crosslines is 50 m.*
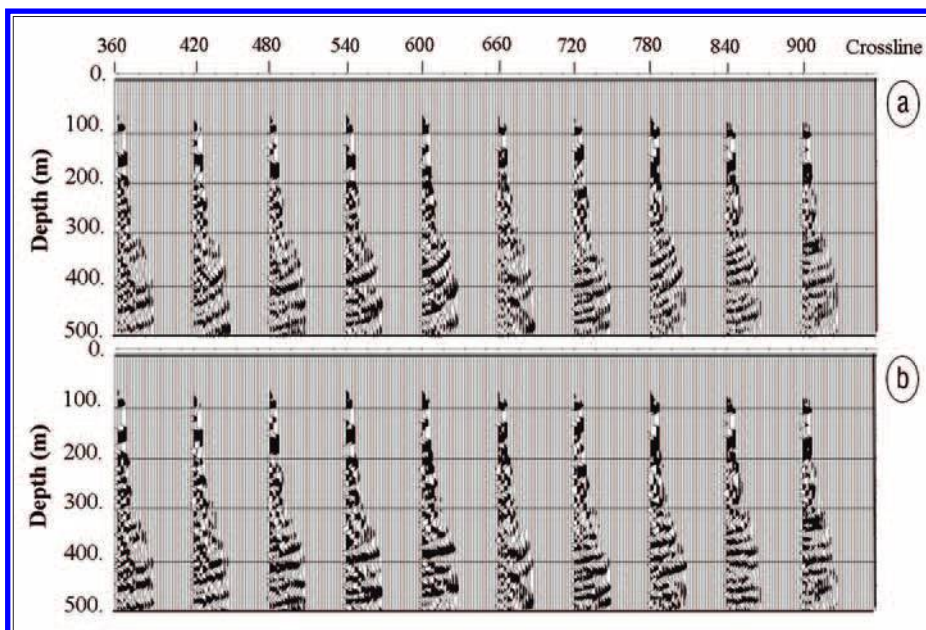


**Figure 2.** *Common-image offset gathers for velocity models before (a) and after (b) inversion. The distance between crosslines is 50 m.*

velocities for vertical propagation at the central inline of the study area. The figure shows dramatic improvement in lateral resolution as a result of the inversion. We assessed the quality of the inversion by comparing modeled shot records for the starting and inverted models with the recorded records. This comparison showed a marked improvement in kinematic agreement as a result of the model update. Kirchhoff prestack depth migration (PSDM) was also used to evaluate the starting and inverted velocity models. Figure 2 compares common-image point (CIP) gathers for both the starting model (upper panel) and the FWI-derived model (lower panel). The gathers between the depths of 200 and 600 m are generally much flatter for the inverted velocity

model. They are not perfectly flat because gather flatness is not measured in the objective function and, perhaps, because of the single-parameter nature of the inversion. Comparison of the corresponding PSDM stacks in Figure 3 also shows a pronounced improvement in image resolution for the model obtained from inversion. In particular, the horizons between 300 and 600 m are much more continuous for the inverted model (lower panel) than for the starting model (upper panel). In addition, the overburden velocity "push-down" effects as seen in the circled areas are also significantly reduced by the inversion.

Finally, in order to assess the accuracy of lateral resolution exhibited in the FWI model, we compared a depth slice
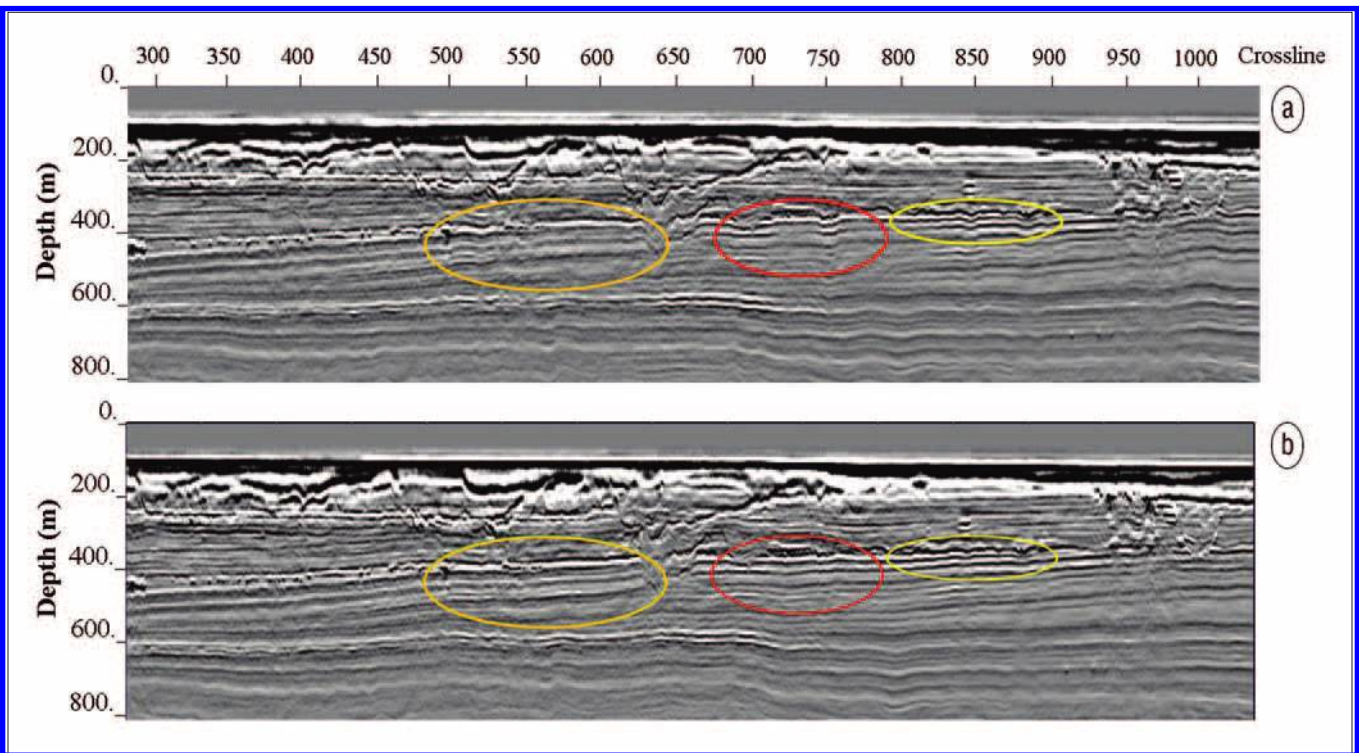


**Figure 3.** PSDM stacked images using velocity models before (a) and after (b) inversion. Different colored circles mark the corresponding areas before and after FWI that show improved images. The updated region extends to a depth of 500 m and the distance between crosslines
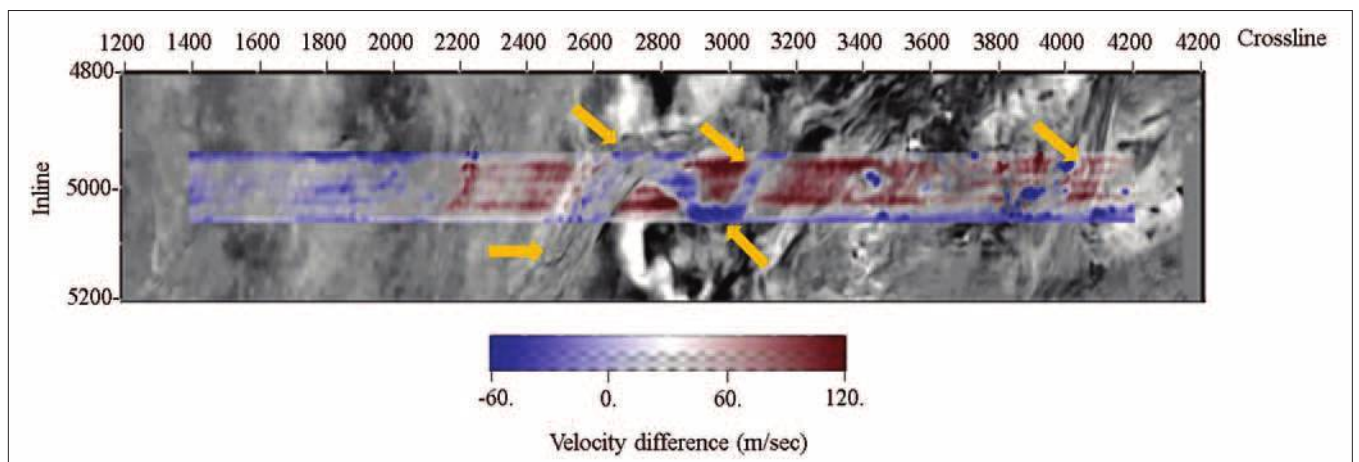


**Figure 4.** Velocity differences between the starting model and inverted model, overlaid on the image from beam PSDM, at a depth of 340 m. Yellow arrows indicate channel locations, and the distance between both inlines and crosslines is 12.5 m.
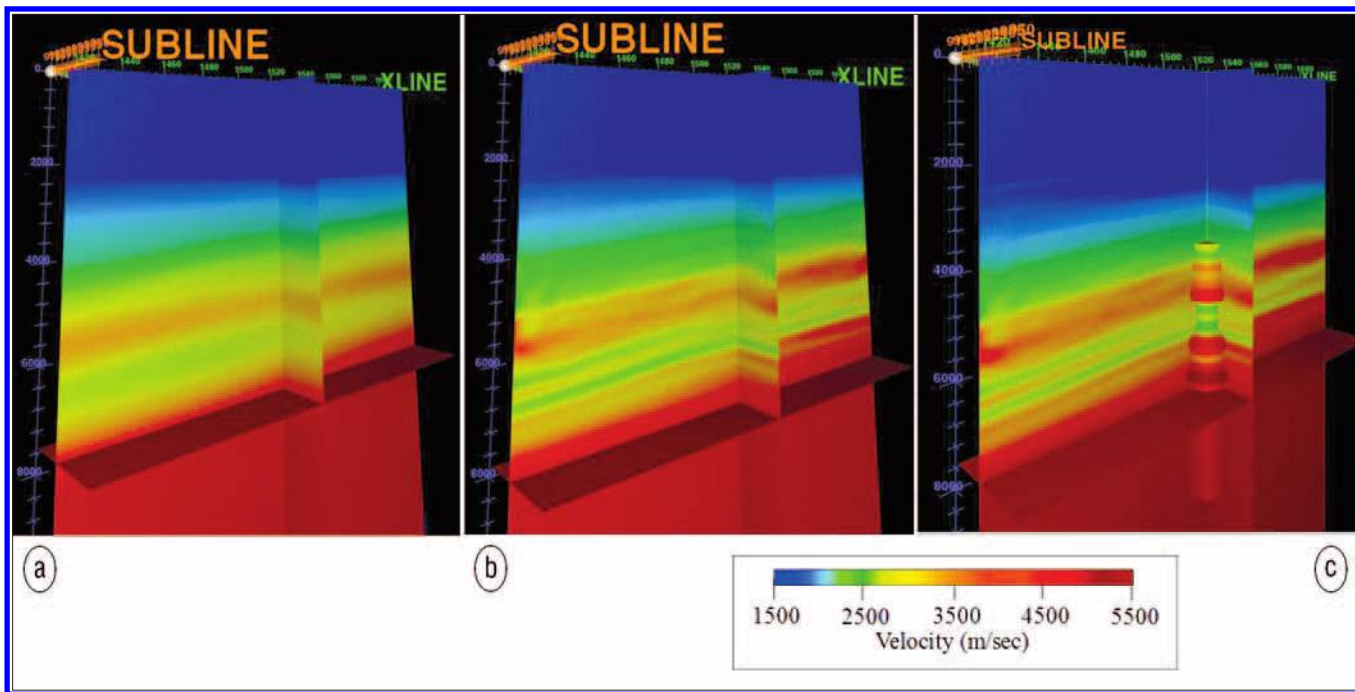
**Figure 5.** *Isotropic velocity for the starting model (a) and inverted model (b), and the inversion result for vertical propagation velocity, after conversion of the isotropic result by Thomsen's δ(z) (c). Well velocities for vertical propagation are superimposed after filtering to the bandwidth of the inversion.*
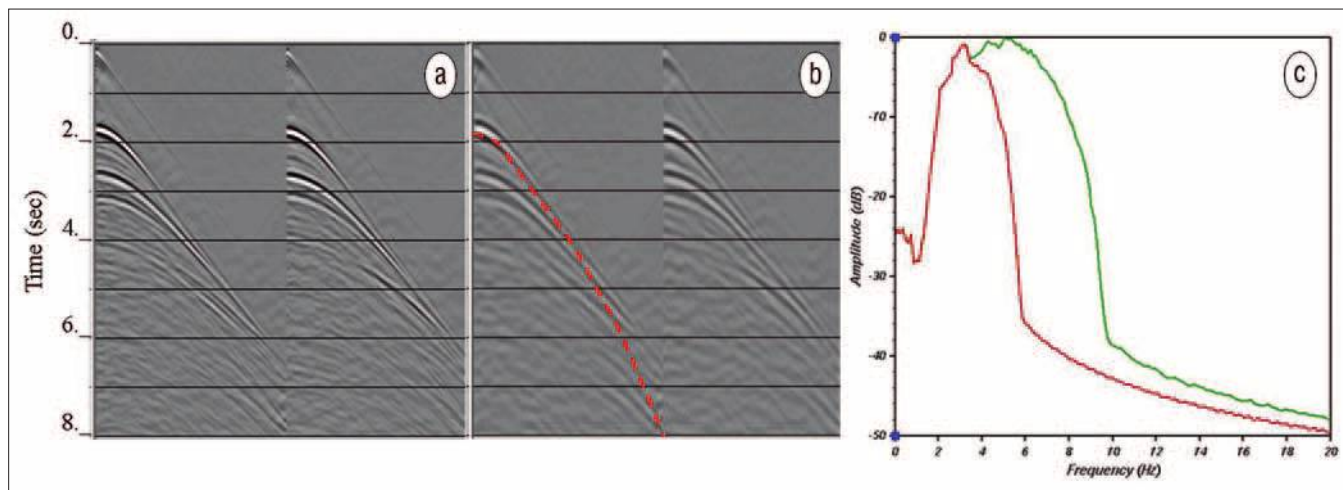


**Figure 6.** *Shot gathers of the fully deghosted data filtered with corner frequencies of 1, 2, 5, and 10 Hz (a) and 1, 2, 3, and 6 Hz (b), which also shows the mute pattern that was applied prior to inversion. (c) The amplitude spectra for (a) (green) and (b) (red).*

from beam PSDM with the inverted velocity model. Figure 4 overlays the velocity difference between the starting model and inverted models, at a depth of 340 m, on a horizontal slice from beam PSDM. The high-resolution velocity updates introduced by FWI correlate with the channels shown in the beam PSDM image quite well, and we can clearly identify the fast and slow channels in the sediments.

### An example of inversion using a preconditioned gradient and far-offset reflections to better resolve deep structure

Our next example demonstrates the application of FWI to improve the resolution of reflectors at a depth of 6 km. The data were acquired in the Gulf of Mexico. Because the water depth was 2.3 km and the maximum inline offset in the

narrow-azimuth spread was 7.4 km, no diving waves were available to illuminate the deep structure. We thus implemented the inversion strategy discussed above for reflections using the method that preconditions the gradient by integrating it over depth (Equation 4). Data preparation for this style of inversion is more involved than that for the shallow-water inversion of refractions, because it entails receiver deghosting, the elimination of free-surface multiples, and the selection of mutes that remove the water-bottom reflection and isolate the farthest half of the offsets for inversion.

The data were acquired using dual-sensor recording, and receiver de-ghosting was performed in the manner discussed by Carlson et al. (2007). The inversion covered approximately 80 km² and spanned a full-power bandwidth of 4–5 Hz.

Because this area is characterized by weak VTI, the inversion was performed under isotropic assumptions. A vertical stretch was subsequently applied to adjust the depths of the inverted model. We used well data to derive an empirical relation between density and velocity, and this was then used to fix density in early inversion attempts by fully-acoustic wave propagation. However, the effects of variable density were eventually deemed to be insignificant for the deeper reflections, and a scalar wave equation was applied in the final inversion.

Figure 5 compares the starting velocity model for the inversion (left panel) with the model obtained by FWI (middle panel). The inversion nicely resolved low-velocity layers with thicknesses of approximately 0.5 km. Depths for the inverted model were then adjusted using a sonic log that was filtered to have the same vertical wavenumber range as the inverted model. The right panel of Figure 5 shows the inverted model after depth adjustment to account for VTI. This adjustment was obtained using a value for the Thomsen parameter "δ" that varied smoothly with depth and did not vary laterally. The comparison with the well log shows good agreement over the entire range of scale sizes inverted.

## An example of Born inversion using only precritical reflections

Under rare circumstances, it is possible to obtain an adequate update of a highly smooth starting model using only the Born scattering kernel. This requires exceptionally clean data at the lowest possible frequencies. In this section, we present the results of an inversion using high-quality data that have also been de-ghosted on both the source and receiver sides. The water column is about 1.3 km deep. The data were acquired in the Møre Margin area in the Norwegian Sea using dual-sensor streamers at 25 m depth, with time and depth-distributed sources at 10 m and 14 m, and a maximum offset of 10,050 m. The implementation of this source array, in conjunction with dual-sensor streamers, allows full de-ghosting of the data (Farouki et al., 2011).

Preprocessing steps for these data were similar to those used for the reflection-based inversion in the previous section, except that the source ghost was also removed. The left and middle panels of Figure 6 show shot records, after noise removal, deghosting and the application of two

sets of bandpass filters. The record in the left panel was filtered over the inversion bandwidth with corner frequencies of 1, 2, 5, and 10 Hz. The middle panel shows the same record after filtering with corner frequencies of 1, 2, 3, and 6 Hz. The corresponding amplitude spectra for each record are shown in the panel on the right. The comparison shows that there are coherent reflected events at frequencies well below 3 Hz. The data were then muted to exclude both the water-bottom reflection and the modeled direct arrival, which can be strong in the absence of source and receiver ghosts. Muting of the modeled and recorded direct arrivals was not strictly necessary, because the associated data residual images in the water column, which is masked. However, our goal was to evaluate the inversion performance for precritical energy, and the ensuing mute pattern naturally excluded these arrivals. The mute pattern is superimposed on the middle panel in Figure 6.
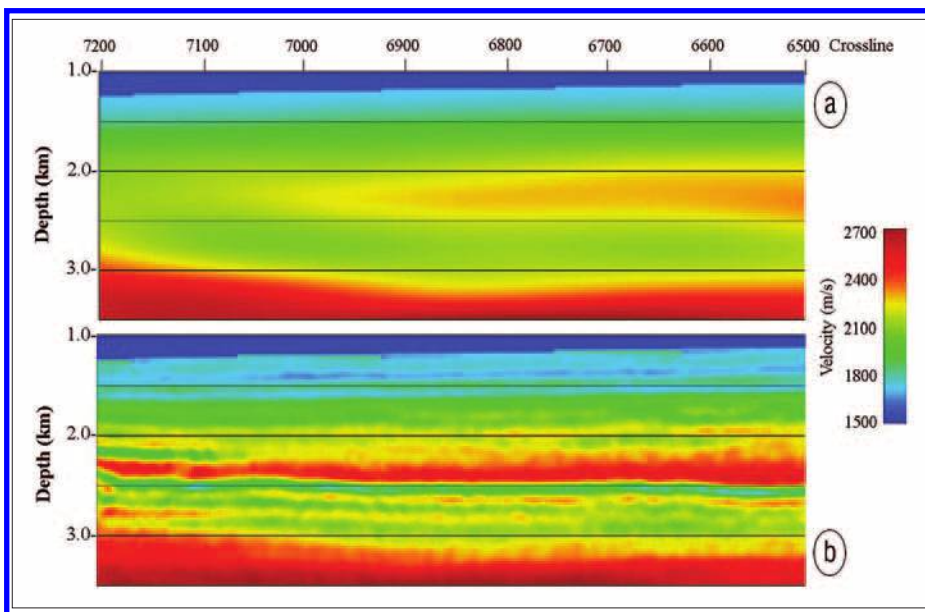


*Figure 7. Starting velocity model for the inversion (a) and inverted model (b). The distance between crosslines is 25 m*
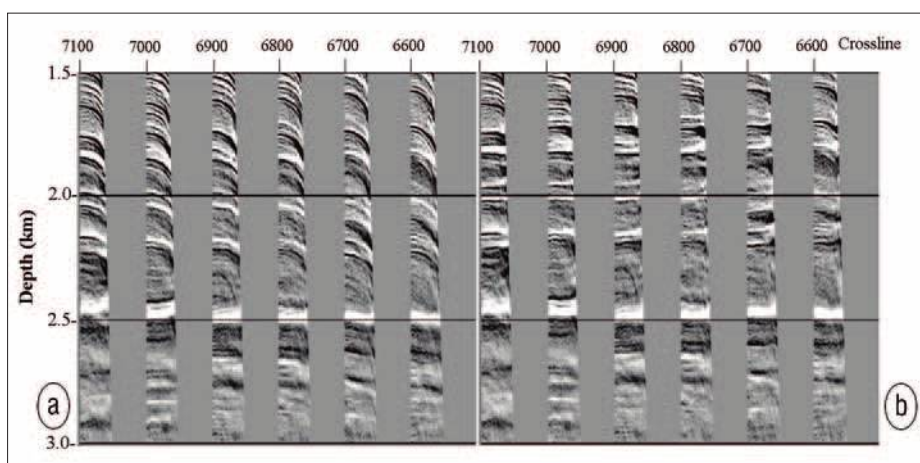


*Figure 8. Kirchhoff PSDM common-image gathers for the starting velocity model (a) and inverted model (b). The distance between crosslines is 25 m.*

The top panel of Figure 7 shows the starting velocity model, which was obtained from velocities used in prestack time migration, and the bottom panel shows the inverted velocity model after 10 iterations. The inverted model exhibits a much higher resolution than the starting model to a depth of 3 km. In order to validate the inversion results, we computed PSDM CIP gathers, and the corresponding stacks, for both the starting and inverted models. The left and right panels of Figure 8 show the gathers for the starting and inverted velocity models, respectively. The depth range for comparison begins at 1.5 km because this is the range over which there was a sufficient range of offsets available after muting. The results show significant improvement in overall flatness of the gathers after inversion. As expected, the corresponding stack for the inverted model in the bottom panel of Figure 9 shows a pronounced improvement in resolution compared with the stack for the starting model in the upper panel. The inversion results are not perfect, in part because of the poor accuracy of the starting model, which led to cycle skips, and because of the restricted range of incidence angles after muting. Nevertheless, they demonstrate that exceptionally clean, low frequencies can enable the Born scattering kernel to inject low wavenumbers during velocity reconstruction.

## Conclusions

We have demonstrated that FWI can be used to resolve shallow channels in a shallow-water environment through the inversion of diving waves and refractions by the Born scattering kernel. We have also shown that in the absence of diving waves and refractions, reflections can be used to resolve low-velocity layers with scale sizes of approximately 0.5 km, at a depth of 6 km. The key elements for this inversion were a boost in low-frequency content provided by receiver-side de-ghosting, together with the application of a preconditioned gradient that suppresses some of the linearity inherent in Born inversion. Finally, we demonstrated that FWI can accurately provide large velocity changes with long spatial wavelengths using the Born scattering kernel, if the data have been de-ghosted on both the shot and receiver sides, and if it contains high signal-to-noise ratio at frequencies as low as 2–3 Hz. *TLE*

## References

Barkved, O., U. Albertin, P. Heavey, J. H. Kommedal, J. P. van Gestel, R. Synnove, H. Pettersen, and C. Kent, 2010, Business impact of full waveform inversion at Valhall: 80th Annual International Meeting, SEG, Expanded Abstracts, 925–929, http://dx.doi.org/10.1190/1.3513929.

Carlson, D., A. Long, W. Sollner, H. Tabti, R. Tengham, and N. Lunde, 2007, Increased resolution and penetration from a towed dual-sensor streamer: First Break, **25**, 71–77.

Farouki, M., A. Long, G. Parkes, and S. Hegna, 2011, Broadband towed marine seismic via total source and receiver de-ghosting: Proceedings of the SEGJ International Symposium.

Gholami, Y., R. Brossier, S. Operto, V. Prieux, A. Ribodetti, and J. Vireaux, 2011, Two-dimensional acoustic anisotropic (VTI) full waveform inversion: the Valhall case study: 81st Annual International Meeting, SEG, Expanded Abstracts, 2543–2548, http://dx.doi.org/10.1190/1.3627720.

Kelly, S., J. Ramos-Martinez, B. Tsimelzon, and S. Crawley, 2010. A method for extracting low frequencies from dual-sensor, field recordings in order to update interval velocity and density: 72nd EAGE Conference & Exhibition, Extended Abstracts, Session A020.

Sheng, J., A. L. Leeds, M. Buddensiek, and G. T. Schuster, 2006, Early arrival waveform tomography on near-surface refraction data: Geophysics, **71**, no. 4, U47–U57, http://dx.doi.org/10.1190/1.2210969.

Sirgue, L., and R. G. Pratt, 2004, Efficient waveform inversion and imaging: A strategy for selecting temporal frequencies: Geophysics, **69**, no. 1, 231–248, http://dx.doi.org/10.1190/1.1649391.

Wu, R. S., and M. N. Toksoz, 1987, Diffraction tomography and multisource holography applied to seismic imaging: Geophysics, **52**, no. 1, 11–25, http://dx.doi.org/10.1190/1.1442237.

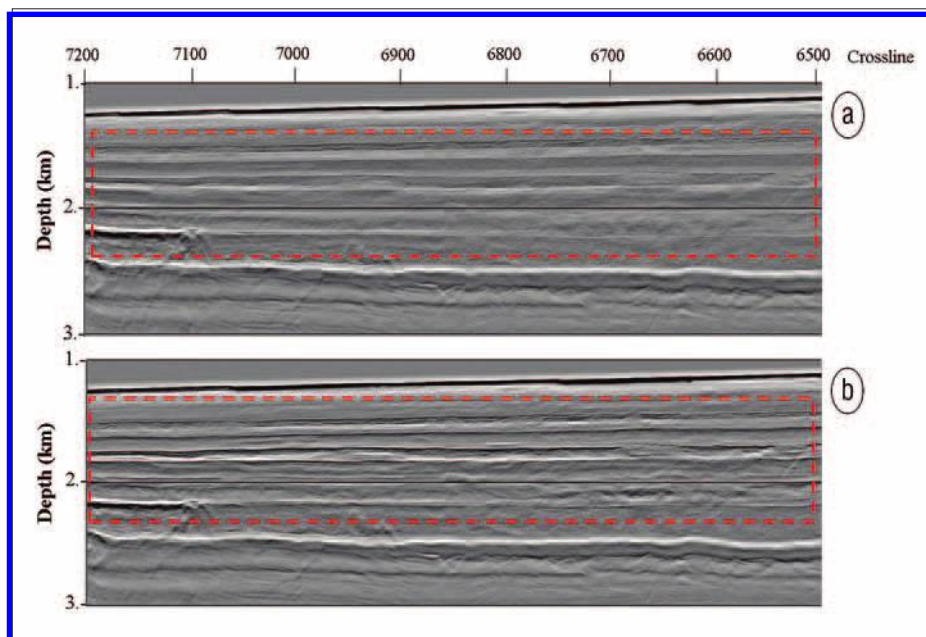*Corresponding author: Steve.Kelly@pgs.com*



**Figure 9.** *Kirchhoff-migrated images for the starting model (a) and the inverted model (b). The distance between crosslines is 25 m. The dashed red box encloses an area over which the horizons and features show a significant improvement in resolution and signal-to-noise ratio.*

**This article has been cited by:**

1. K. A. InnanenReconciling seismic AVO and precritical reflection FWI - Analysis of the inverse Hessian 1022-1027. [Abstract] [References] [PDF] [PDF w/Links]